Supplementary Information for

High-performance and durable anion-exchange membrane water electrolysers with high-molecular-weight polycarbazole-based anion-conducting polymer

Sungjun Kim,[a,‡] Seok Hwan Yang,[a,b,‡] Sang-Hun Shin,[a] Hye Jin Cho,[a] Jung Kyu Jang,[a] Tae Hoon Kim,[a,b] Seong-Geun Oh,[b] Tae-Ho Kim,[a] HyukSu Han,[c] and Jang Yong Lee*[a]

[1]Hydrogen Energy Research Center, Korea Research Institute of Chemical Technology, Daejeon 34114, Republic of Korea

[2]Department of Chemical Engineering, Hanyang University, Seoul 047693, Republic of Korea

[3]Department of Energy Science, Sungkyunkwan University, Suwon 16419, Republic of Korea

‡These authors contributed equally to this work

*Corresponding author: ljylee@krict.re.kr

Table of contents

Supplementary Methods

Polymer synthesis

Materials. 9-(6-Bromohexyl)-9H-carbazole (BHC) and 1,6-di(9H-carbazol-9-yl)hexane (DHC) were synthesised as described elsewhere[1,2]. Trifluoromethanesulfonic acid (TFSA), methylene chloride (MC), trimethylamine (TMA) solution, and *N,N*-dimethylformamide (DMF) were supplied by Sigma-Aldrich (USA). 1,1,1-Trifluoroacetone (TFA) was supplied by Thermo Fisher Scientific (USA). KOH, methanol, ethanol, and isopropanol were purchased from Samchun Pure Chemicals (South Korea). All chemicals were used as received.

Monomer synthesis. Carbazole was poured into a completely dry 500 mL three-neck flask equipped with a magnetic bar under Ar, and DMF was added to obtain a homogeneous solution. The flask was cooled to 0 °C, charged with KOH, and then dropwise supplemented with 1-bromohexane under vigorous stirring. The reaction was allowed to proceed at room temperature for 48 h, and the mixture was then poured into deionised water:MC (1.5:2, v/v). The organic layer containing the product was separated and washed with brine, and the remaining moisture was removed using $MgSO_4$. After filtration and solvent evaporation, the product was recrystallised from methanol to obtain 9-hexyl-9*H*-carbazole (HC) as a white needle-like powder. ^{1}H NMR (500 MHz, $CDCl_3$) δ (ppm): 8.00 (H_d), 7.37 (H_c), 7.31 (H_a), 7.12 (H_b), 4.18 (H_e), 1.77 (H_f), 1.29–1.20 ($H_g, H_{g'}, H_h$), and 0.78 (H_i).

Synthesis of high-molecular-weight polycarbazole-based backbone (poly(9-(6-bromohexyl)-9H-carbazole-co-1,1,1-trifluoroisopropane-co-9-hexyl-9H-carbazole) (HPC-br-x)). BHC (111.50 g, 337.60 mmol / 89.30 g, 270.39 mmol / 72.50 g, 219.52 mmol for HPC-br-2.4/2.0/1.6, respectively) and HC (0 g, 0 mmol / 16.99 g, 67.60 mmol / 29.71 g, 118.20 mmol for HPC-br-2.4/2.0/1.6, respectively) were charged into a flame-dried 1 L three-neck flask equipped with an overhead mechanical stirrer and dissolved in MC. The solution was placed in an ice bath at 0 °C, incubated for 30 min, slowly supplemented with TFA (51 .07 g, 455.76 mmol / 51.15 g, 456.47 mmol / 51.08 g, 455.92 mmol for HPC-br-2.4/2.0/1.6, respectively) and TFSA (TFSA, 500g, 3332.22 mmol) under continuous stirring, cooled for 3 h, warmed to room temperature, and maintained at this temperature for 72 h. After 24 h, DCH (chain extender, 0.56 g, 1.34 mmol / 0.53 g, 1.28 mmol / 0.51 g, 1.23 mmol) was added via syringe injection. The resulting viscous dark brown mixture was precipitated in fresh methanol, and the fibre-like product was filtered, washed with hot methanol, and dried at 80 °C in a vacuum oven for 24 h. HPC-br-2.4; ^{1}H NMR (500 MHz, DMF-*d*[7]) δ (ppm): 8.43 (H_c), 7.58 (H_a), 7.35 (H_b), 4.37 (H_d), 3.43 (H_g), 2.18 (H_h), 1.88–1.67 ($H_{e'}, H_e$), and 1.49–1.29 ($H_{f'}, H_f$). HPC-br-2.0; ^{1}H NMR (500 MHz, $CDCl_3$) δ (ppm): 8.10 (H_c), 7.21 (H_a), 7.16 (H_b), 4.11 (H_d), 3.22 (H_g), 2.07 (H_h), 1.76–1.68 ($H_{e'}, H_e$), 1.34–1.29 ($H_{f'}, H_f$), 1.19 (H_i), and 0.75 (H_j). HPC-br-1.6; ^{1}H NMR (500 MHz, DMF-*d*[7]) δ (ppm): 8.43 (H_c), 7.57

(H$_a$), 7.36 (H$_b$), 4.37 (H$_d$), 3.43 (H$_g$), 2.18 (H$_h$), 1.88–1.68 (H$_{e'}$, H$_e$), 1.52–1.32 (H$_{f'}$, H$_f$), 1.23 (H$_i$), and 0.78 (H$_j$).

Quaternisation (polycarbazole-based poly(9-(6-(trimethylammonium bromide)hexyl)-9H-carbazole-co-1,1,1-trifluoroisopropane-co-9-hexyl-9H-carbazole) (HQPC-TMA-x)). A three-necked flask was charged with HPC-br-*x* (40.00 g) and DMF (127 mL), and the solution was then slowly supplemented with 45 wt% aqueous TMA (43 mL, 282.81 mmol / 36.31 mL, 234.98 mmol / 32.72 mL, 211.73 mmol for HQPC-TMA-2.4/2.0/1.6, respectively) and stirred at room temperature for 24 h. The product was precipitated using fresh isopropanol, filtered off, washed several times, and dried under vacuum at 60 °C for 24 h. HQPC-TMA-2.4; ¹H NMR (500 MHz, DMSO-*d$_6$*) δ (ppm): 8.41 (H$_c$), 7.59 (H$_a$), 7.22 (H$_b$), 4.38 (H$_d$), 3.28 (H$_g$), 3.04 (H$_j$), 2.20 (H$_h$), 1.90–1.53 (H$_{e'}$, H$_e$), and 1.51–1.19 (H$_{f'}$, H$_f$). HQPC-TMA-2.0; ¹H NMR (500 MHz, DMSO-*d$_6$*) δ (ppm): 8.41 (H$_c$), 7.57 (H$_a$), 7.20 (H$_b$), 4.36 (H$_d$), 3.25 (H$_g$), 3.01 (H$_k$), 2.20 (H$_h$), 1.90–1.55 (H$_{e'}$, H$_e$), 1.45–1.22 (H$_{f'}$, H$_f$), 1.19 (H$_i$), and 0.75 (H$_j$). HQPC-TMA-1.6; ¹H NMR (500 MHz, DMSO-*d$_6$*) δ (ppm): 8.38 (H$_c$), 7.57 (H$_a$), 7.22 (H$_b$), 4.35 (H$_d$), 3.24 (H$_g$), 3.01 (H$_k$), 2.18 (H$_h$), 1.90–1.55 (H$_{e'}$, H$_e$), 1.48–1.25 (H$_{f'}$, H$_f$), 1.19 (H$_i$), and 0.76 (H$_j$).

NMR spectroscopy. Chemical structures of the synthesised extender and carbazole-based copolymers were confirmed using NMR spectroscopy. ¹H and ¹³C NMR spectroscopy spectra (Brüker DRX500, Brüker Corporation, Billerica, MA, USA) were recorded at 500.13 and 75 MHz, respectively) in CDCl$_3$ (δ ¹H = 7.26 ppm), DMSO-*d$_6$* (δ ¹H = 2.50 ppm), and DMF-*d$_7$* (δ ¹H = 2.75, 2.95, and 8.03 ppm) as solvents.

Polymer characterisation

Gel permeation chromatography (GPC). The molecular weights and polydispersity indices (PDIs, Đ) of the synthesised polymers were measured using a GPC instrument (Waters Breeze, USA) equipped with Shodex KF-805L columns and a Waters 2414 refractive index detector. Tetrahydrofuran was used as the mobile phase. The system was operated at 40 °C and a flow rate of 1 mL min⁻¹. A polystyrene standard was used as a reference.

Polymer viscosity. Cannon-Fenske Routine Viscometers were used to the relative viscosity(η_{rel}), specific viscosity(η_{sp}), reduced viscosity(η_{red}), inherent viscosity (η_{inh}) and intrinsic viscosity ([η]) of the polymer solutions in DMSO containing 0.05M LiBr (0.3 to 0.7 g L⁻¹) at 25 °C. The sample solutions were passed through a 5 µm PTFE filter prior to measurements. To maintain a constant temperature of 25 °C, all measurements were carried out in a precise-viscosity water bath. The polymer viscosity was calculated as

$$\eta_{rel} = \frac{t}{t_0} \quad (1)$$

$$\eta_{sp} = \frac{t - t_0}{t_0} \quad (2)$$

$$\eta_{red} = \frac{\eta_{sp}}{c} \quad (3)$$

$$\eta_{inh} = \frac{\ln \eta_{rel}}{c} \quad (4)$$

$$[\eta] = \lim_{c \to 0} \frac{\eta_{sp}}{c} \quad (5)$$

where η is the solution viscosity, t_0 is the flow time of solvent, t is the flow time of solution, and c is the mass concentration of the polymer. In a plot of $[\eta]$ versus c, the y-intercept was obtained by extrapolating the η_{red} and η_{inh} to c = 0. The intrinsic viscosity was obtained by calculating the average of the obtained y-intercept values.

Ion-exchange capacity (IEC) measurements. An automatic titrator (Metrohm 794 Basic Titrino) was used to determine the IEC (meq g^{-1}) by Mohr titration. The membrane in the Cl$^-$ form was immersed into aqueous Na$_2$SO$_4$ (1 M, 100 mL) for 24 h, and the released Cl$^-$ ions were titrated using 0.01 M AgNO$_3$. To obtain accurate IEC values, the procedure was repeated three times for each sample. The weight-based IEC of the Cl$^-$-form membrane was calculated as

$$IEC_w^{Cl^-} \ (meq \ g^{-1}) = (C_{AgNO_3} \times \Delta V_{AgNO_3})/W_d \quad (6)$$

where C_{AgNO_3} is the concentration of the AgNO$_3$ solution, ΔV_{AgNO_3} is the consumed volume of this solution, and W_d is the weight of dry membrane.

The volume-based IEC of OH$^-$-form membranes in dry and wet states was calculated as

$$IEC_v^{OH^-} \ (dry) \ (meq \ cm^{-3}) = IEC_w^{OH^-} \times \delta_d \quad (7)$$

$$IEC_v^{OH^-} \ (wet) \ (meq \ cm^{-3}) = IEC_v^{OH^-} \ (dry) \ / \ (1 + 0.01WU(vol\%)) \quad (8)$$

where δ_d is the membrane density in the dry state.

Water uptake (WU) and dimensional change. Membranes in the Br$^-$-form (3 cm × 3 cm) were converted to the OH$^-$ form by immersion into 1 M KOH at room temperature for 24 h. The weight (

W_w), thickness (t_w), length (l_w), and volume (v_w) of the fully hydrated membranes were measured after gently wiping excess water off their surface with tissue paper. The ion-exchanged membranes (OH⁻ form) were dried in a vacuum oven, and their weight (W_d), thickness (t_d), length (l_d), and volume (v_d) were measured. The dried membranes were immersed into deionised water for 24 h at various temperatures (25–80 °C). After wiping excess water off the surface of the fully hydrated membranes with tissue paper, their weight (W_w), thickness (t_w), length (l_w), and volume (v_w) were measured. The volumes of dry and wet membranes were calculated from their dimensions. WU and dimensional changes were calculated as

$$WU\ (\%) = (W_w - W_d)/W_d \times 100\% \tag{9}$$

$$\Delta t = \frac{t_w - t_d}{t_d}, \tag{10}$$

$$\Delta l = \frac{l_w - l_d}{l_d}, \tag{11}$$

$$\Delta v = \frac{v_w - v_d}{v_d}. \tag{12}$$

The volume-based WU (vol%) was determined by considering the weight of the membrane and its density in the dry state:[3]

$$WU\ (vol\%) = \frac{W_w - W_d}{W_d} \times \frac{\delta_d}{\delta_w} \times 100\%, \tag{13}$$

where δ_d is the membrane density in the dry state, and δ_w is the density of water.

Gas permeability. The permeabilities of the membranes to H_2 gas were measured at 25 and 60 °C using gas chromatography. After the membranes had been activated in the respective gases (Ar and H_2) for 30 min, the measurements were performed for 2 min (H_2). H_2 was detected within 30 s. Gas permeability P (barrer) was calculated as

$$P = (C_g \times v \times t) / (A \times \Delta p) \tag{14}$$

where C_g is the concentration of the permeated gas (H_2), v is the Ar flow rate at STP (2750 mL/min), t is the membrane thickness, A is the active area (7.5 cm²), and Δp is the gas partial pressure difference across the membrane.

Ionic conductivity measurement. To investigate the in-plane OH⁻ conductivity, we mounted the HQPC-TMA-x membranes (30 μm) on a membrane test system (BT-512, BekkTech) and exposed them

to a continuous flow of N_2 (99.999%) at 400 mL min^{-1} at a constant relative humidity of 100% and 25–80 °C. A constant direct current of 100 μA (ZIVE SP3, WonATech) was applied to the membrane for 30 h until saturation to exchange HCO_3^- and CO_3^{2-} for OH^- (by producing OH^- at the positive electrode through water electrolysis). The membrane's ionic resistance was measured every 30 min using a standard four-probe technique until ion-exchange was saturated. Electrochemical impedance spectroscopy (EIS) measurements were performed using an impedance analyser at an open-circuit voltage over a frequency range of 0.1–20 kHz. Ionic conductivity was calculated as

$$Ionic\ conductivity\ (mS\ cm^{-1}) = \frac{l}{R \times S}, \quad (15)$$

where l is the distance between the electrodes, R is the membrane impedance, and S is the cross-sectional surface area of the membrane.

Small-angle X-ray scattering (SAXS). SAXS (PLS-II 3C beamline, Pohang Accelerator Laboratory, PAL) measurements were performed in water at room temperature. The scattering vector q was calculated as

$$q = 4\pi/\lambda \times \sin 2\theta, \quad (16)$$

where λ is the wavelength of Cu K_α radiation (1.542 Å), and 2θ is the scattering angle. The interdomain spacing (d) was calculated as

$$d = 2\pi/q_{max}. \quad (17)$$

Note S1. Synthesis and characterisation of AEMs

Design principle and structural characterisation of HQPC-TMA-*x*

Carbazole, featuring two benzene rings fused to the opposite sides of a pyrrole ring, is a well-studied tricyclic aromatic compound. Carbazole-based polymers exhibit outstanding chemical stabilities, and their high backbone curvatures result in high solubilities in various organic solvents. Previously, we synthesised a polycarbazole-based AEM (QPC-TMA), which, however, had a low molecular weight, because the weak electron-withdrawing ability of carbazole derived from the nitrogen atom resulted in weakened reactivity[1]. To improve the suboptimal physical and mechanical properties and chemical stability of QPC-TMA due to its low molecular weight[4,5], the molecular weight of the polymer backbone was increased by introducing a small amount of a chain extender. Moreover, considering the harsh conditions of water electrolysis, the present study used hexyl spacer–tethered trimethylammonium moieties as anion-conducting groups. Furthermore, three controlled-IEC AEMs (HQPC-TMA-1.6, -2.0, and -2.4) were prepared by introducing a hexylcarbazole monomer without anion-conducting groups.

During polymerisation, 0, 25, and 54 mol% of HC was added to BHC to adjust the IEC of the polymer backbone, poly(9-(6-bromohexyl)-9*H*-carbazole-co-1,1,1-trifluoroisopropane-co-9-hexyl-9*H*-carbazole) (HPC-br-*x*; *x* = theoretical IEC). The synthesis of HPC-br-*x* was confirmed using ^{1}H NMR spectroscopy. The molecular weights of HPC-br-*x* and PC-br (polymer synthesised without DCH) were measured by GPC. The number- and weight-average molecular weights of HPC-br-1.6, HPC-br-2.0, and HPC-br-2.4 (M_n = 65, 89, and 78 kDa; M_w = 307, 343, and 312 kDa, respectively) were approximately three times higher than those of PC-br (M_n = 23 kDa and M_w = 87 kDa). After quaternisation, the IEC values of HQPC-TMA-1.6, -2.0, and -2.4 were determined as 1.6, 1.9, and 2.3 meq g^{-1}, respectively, using the titration method. The intrinsic viscosities of HQPC-TMA-1.6, -2.0, and -2.4 (1.2, 1.3, and 1.1, respectively) exceeded those of QPC-TMA (0.7). This observation is consistent with the trends observed in the GPC molecular weight results. The alignment between the intrinsic viscosity data and the GPC molecular weight outcomes underscores the reliability of our findings and supports our conclusions regarding the polymer's structural characteristics and its impact on solution behavior. This correlation further strengthens our hypothesis and provides a comprehensive understanding of the polymers under investigation.

Water molecules in AEMs can affect the formation of anion-transport channels. The excessive absorption of water results in the substantial deterioration of the chemical, physical, and mechanical properties of AEMs. Consequently, a suitable WU is critical for realising AEMs with acceptable anion conduction and mechanical properties. **Fig. S10** presents the WU values of HQPC-TMA-*x*'s, QPC-TMA, and PiperION (commercial AEM) determined at 25, 40, 60, and 80 °C. As expected, the WU values and dimensional variations of HQPC-TMA-*x*'s increased with increasing IEC. Compared to

HQPC-TMA-2.4 (which had an almost identical chemical structure and IEC), QPC-TMA showed a higher WU and dimensional variation in all temperature ranges. Notably, QPC-TMA exhibited over a two times higher WU and dimensional variation at 80 °C, which could stem from physical property enhancement due to the entanglement of the polymer main chains.

Alkaline stability test

The TMA group is mainly degraded via Hofmann elimination and demethylation. As shown in **Fig. 3b**, the degradation of the immersed HQPC-TMAx films was examined using ^{1}H NMR spectroscopy every 500 h. Even after 2,500 h, the ^{1}H NMR spectra of the three membranes did not show any signs of degradation. Although a new peak attributable to the Hofmann elimination reaction was observed at 5.5 ppm, it was negligible. After the 2,500 h test, the counter anion within the HQPC-TMA-x's was exchanged from OH^- to Cl^- for a precise evaluation of anion conductivity without CO_2 influence. This modification was necessary to exclude the effects of HCO_3^- or CO_3^{2-} ions (readily formed from OH^- and CO_2 in the ambient air) on measurement accuracy. Throughout the entire stability test, all members of the HQPC-TMA series consistently exhibited Cl^- conductivity.

H$_2$ permeability

H$_2$ permeability is crucial factor to be considered for AEMs and ionomers. Typically, anion-conducting polymers (ACPs) are used not only as membrane materials, but also as ionomers. The high H$_2$ permeability of a given membrane can lead to leakage of current and decrease the efficiency of the single cell. Whereas, the high H$_2$ permeability of the ionomer can enhance cell performance by facilitating out-gassing in the electrodes. Therefore, a certain optimal H$_2$ permeability is required for a given ACP to be used as both an ionomer and membrane material. As shown in **Fig. S13**, HQPC-TMA-1.6 showed a lower H$_2$ permeability than PiperION at 25 and 80 °C. Compared with PiperION, HQPC-TMA-2.0 featured a lower H$_2$ permeability at 25 °C and almost identical H$_2$ permeability at 80 °C. However, HQPC-TMA-2.4 showed a higher H$_2$ permeability than PiperION. Although the difference was overly small at 25 °C, the H$_2$ permeability of HQPC-TMA-2.4 was over two times that of PiperION at 80 °C. Despite the relatively high H$_2$ permeability of HQPC-TMA-2.4, considering other commercial AEMs (sustainability), this permeability could be appropriate for use as both a membrane material and ionomer. Interestingly, compared with PiperION, HQPC-TMA-x's showed a larger H$_2$ permeability change upon going from 25 to 80 °C, which could stem from the corresponding morphology differences. In particular, as mentioned in the main text, HQPC-TMA-2.4 had a better-developed morphology than PiperION while showing an almost identical IEC. Considering that H$_2$ gas can be transferred via ion-conducting channels, the higher H$_2$ permeability of HQPC-TMA-2.4 was ascribed to the easy transfer of H$_2$ molecules via the well-interconnected ionic channels of this ACP.

Note S2. Overpotential analysis on AEMWEs with different AEM/AEI combination

An analysis of overpotentials was conducted to determine the source of the enhanced performance exhibited by the HQPC-TMA-2.4 based cell, as compared to commercial benchmark cells employing PiperION. Typically, the total cell overpotential (η_{cell}) is simply broke down into the three major overpotentials (kinetic overpotential (η_{kin}), Ohmic overpotential (η_{Ohm}), and mass transport overpotential (η_{mt}))

$$\eta_{cell} = \eta_{kin} + \eta_{Ohm} + \eta_{mt}$$

The Ohmic overpotential was determined by measuring the high-frequency resistance (HFR) at various current densities, which represents the total electronic resistance of the cell.

$$\eta_{ohm} = j\left(A\ cm^{-2}\right) \times HFR\left(\Omega\ cm^2\right)$$

The kinetic overpotential was extracted from the iR-corrected polarization using simple Tafel model.

$$\eta_{kin} = b \times log\boxed{?}\left(\frac{i}{i_0}\right)$$

The mass transport overpotential was calculated by subtracting the kinetic and Ohmic overpotentials from the measured cell overpotential. As illustrated in **Fig. S15**, despite employing a membrane 1.5 times thicker, the HQPC-TMA-2.4 cell demonstrated an η_{Ohm} comparable to that of the benchmark cell, which utilises a 20 μm–thick PiperION membrane. This observation suggests that the HQPC-TMA-2.4 AEM exhibits superior through-plane OH⁻ conductivity compared to the benchmark AEM under actual operating conditions. This inference is further supported by the notable increase in ohmic overpotential observed in cells when employing thicker 40 μm PiperION membranes. In addition, the AEMWEs with HQPC-TMA-2.4 ionomer (cell #6 and #7) showed lower kinetic and mass transport overpotentials compared to the AEMWEs with PiperION ionomer (cell #4 and #5), underscoring the effectiveness of HQPC-TMA-2.4 as an ionomer. This result is further supported by the electrochemical impedance spectroscopy (EIS) analysis, which revealed that the charge-transport resistances (R_{CT}) of the HQPC-TMA-2.4 cells were lower than those of its PiperION counterparts at all measured current densities (**Fig. S14**). For instance, at a low current density of 0.5 A cm⁻², the R_{CT} of the HQPC-TMA-2.4 cell (73.5 mΩ cm²) was 26.9% lower than that of the PiperION cell (100.4 mΩ cm²). Similarly, at a high current density of 5.0 A cm⁻², the R_{CT} of the HQPC-TMA-2.4 cell (18.2 mΩ cm²) was 13.7% lower than that of the PiperION cell (21.1 mΩ cm²). AEMWEs with the same electrode show similar R_{CT} to each other. The reduced kinetic overpotential observed in the HQPC-TMA-2.4-based electrodes can be attributed to the low phenyl adsorption characteristic of the poly(carbazole)-based backbone. Similarly, the diminished mass transport overpotential is ascribed to the higher gas permeability of HQPC-TMA-2.4, which is favourable for outgassing (**Fig. S16**).

Note S3. Measurement of R_{Others}

Definition of R_{others}:

High frequency resistance (HFR; denoted R_{ohm}) of single cell measured through electrochemical impedance spectroscopy (EIS) encompasses a broader range of resistive factors within the operational environment of an electrolysis cell. These factors include the ion transport resistance through the electrolyte membrane ($R_{ion, AEM}$) and membrane/catalyst layer (CL) interface ($R_{ion, AEM/CL}$), electrical resistance through cell hardware and wiring (ex. $R_{elec, PTL}$, $R_{elec, Flow plate (FP)}$, $R_{elec, Current collector (CC)}$, $R_{elec, wiring}$), and electrical contact resistances between various cell components (ex. $R_{elec, CL/PTL}$, $R_{elec, PTL/FP}$, $R_{elec, FP/CC}$) (**Fig. S25**). Of these, R_{others} encompasses all resistive components except ionic resistance across the AEM ($R_{ion, AEM}$) and contact resistances between the AEM/CL ($R_{ion, AEM/CL}$) and CL/PTL interfaces ($R_{elec, CL/PTL}$) (**Fig. S25b**).

Measurement of R_{others}:

To quantify R_{others} and understand its contribution to the overall HFR (R_{ohm}) increase, particularly due to the corrosion of cell hardware, we conducted a specific test. As shown in **Figure R3b**, we assembled the cell without the membrane and catalyst layers, thus focusing exclusively on the electrical resistances originating from the cell hardware materials, wires, and contact resistances among other cell components. Subsequently, the cell setup for R_{others} measurement was subjected to electrochemical impedance spectroscopy (EIS) at the same operational temperature used for the electrolysis cell experiments. Since this test setup does not involve electrochemical reactions, the impedance measurements primarily capture ohmic resistance, with no capacitive curve observed besides the inductive curve attributable to wiring (**Fig. 5c**).

Supplementary Figures

BHC	HC	IEC
10	0	2.4
8	2	2.0
6.5	3.5	1.6
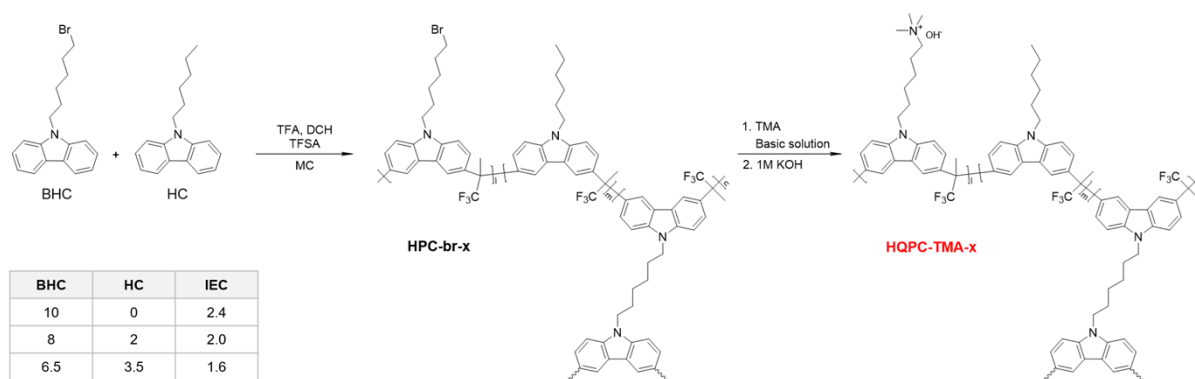
Fig. S1 Synthetic routes of HQPC-TMA-x's

10
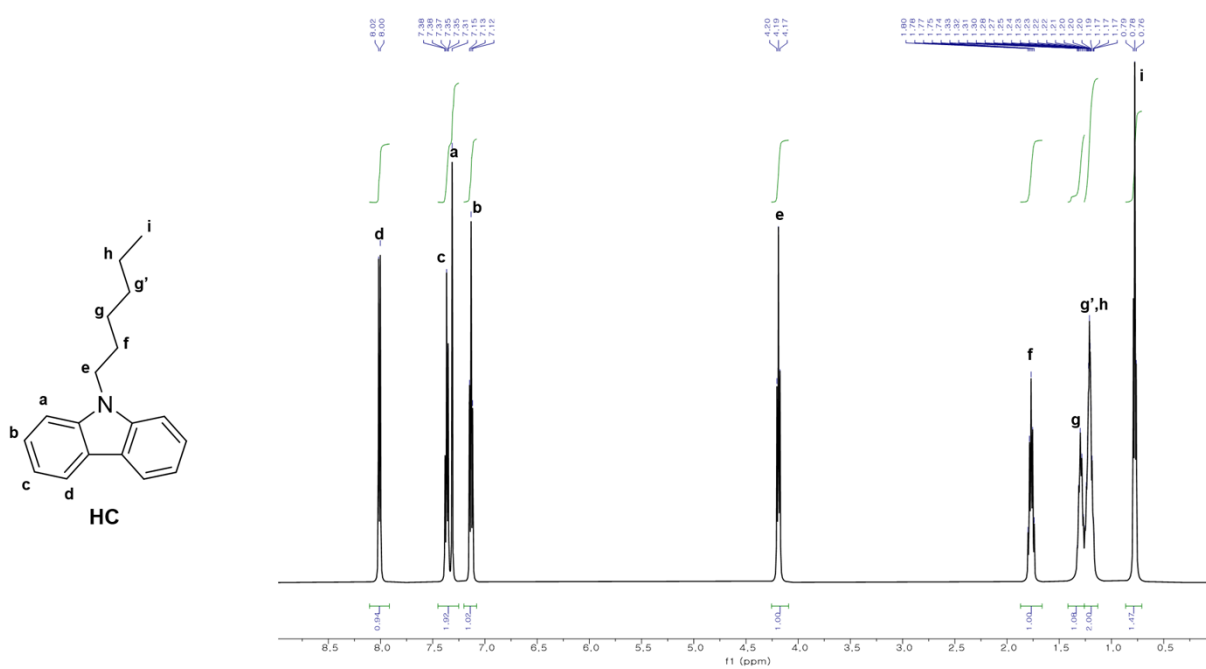
Fig. S2 ^{1}H NMR spectrum of HC

Fig. S3 ^{1}H NMR spectrum of Extender
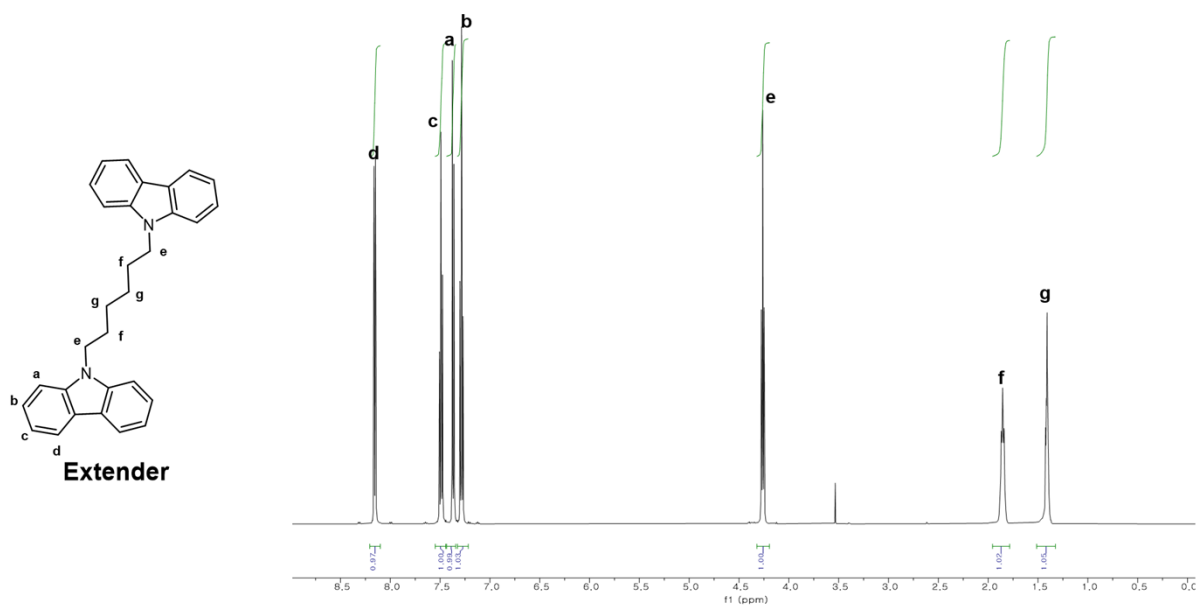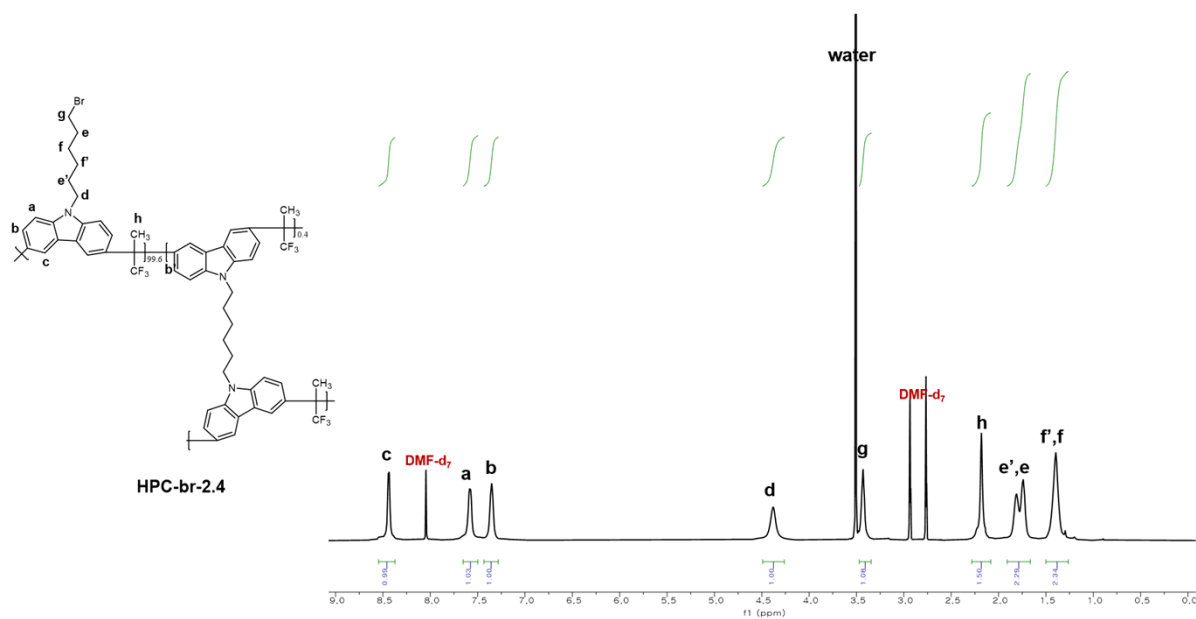
Fig. S4 ^{1}H NMR spectrum of HPC-br-2.4
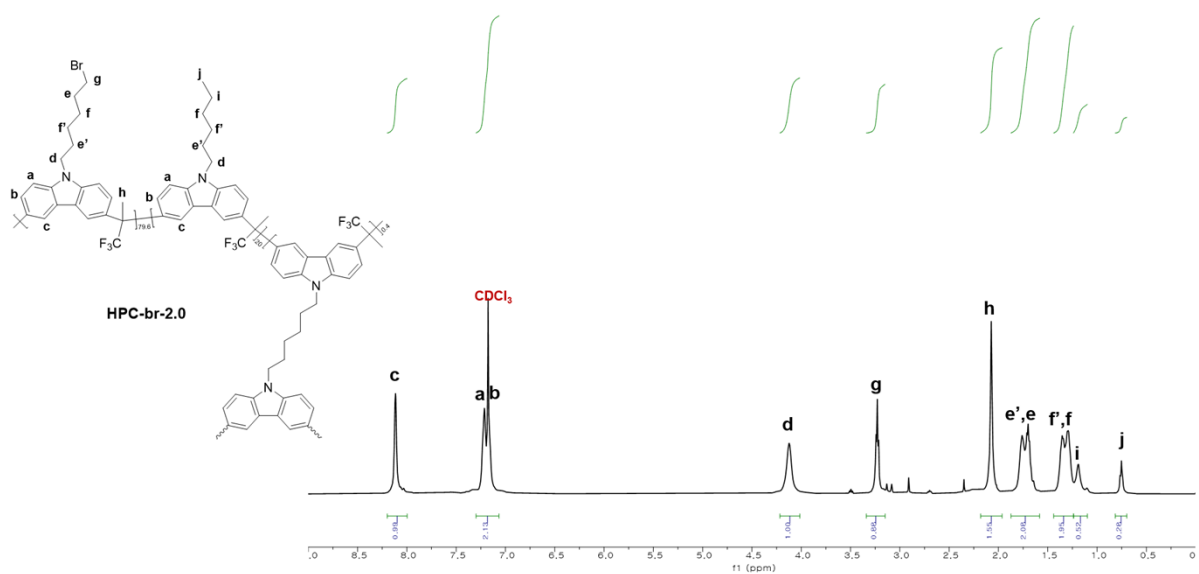
Fig. S5 ^{1}H NMR spectrum of HPC-br-2.0

Fig. S6 ^{1}H NMR spectrum of HPC-br-1.6

Fig. S7 ^{1}H NMR spectrum of HQPC-TMA-2.4

13
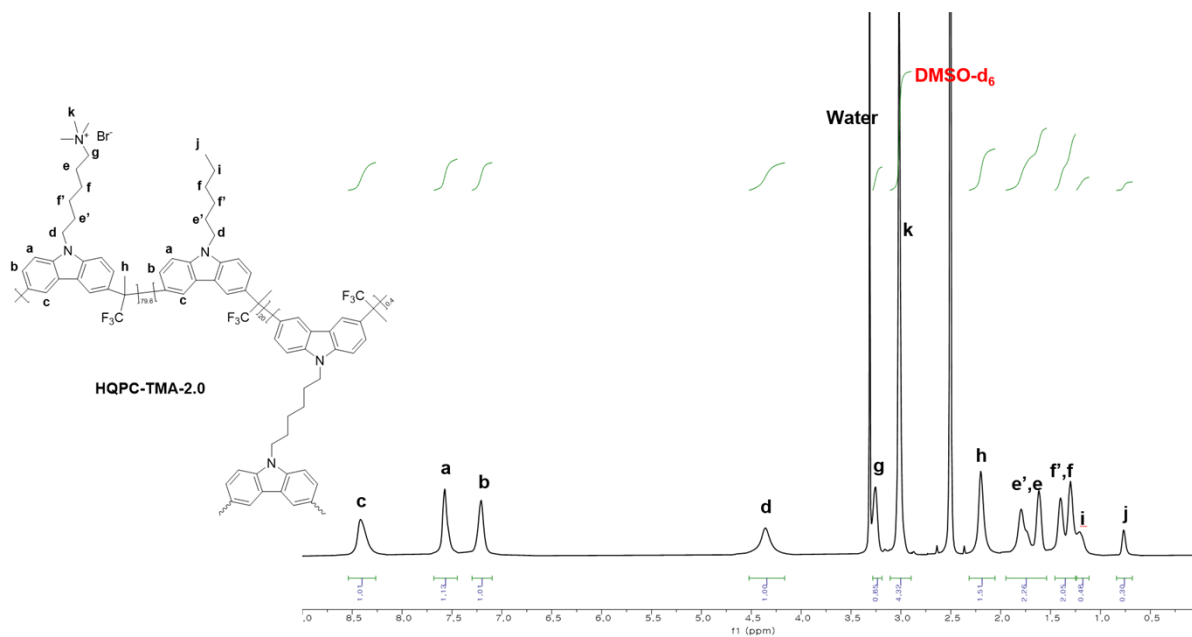
Fig. S8 ^{1}H NMR spectrum of HQPC-TMA-2.0
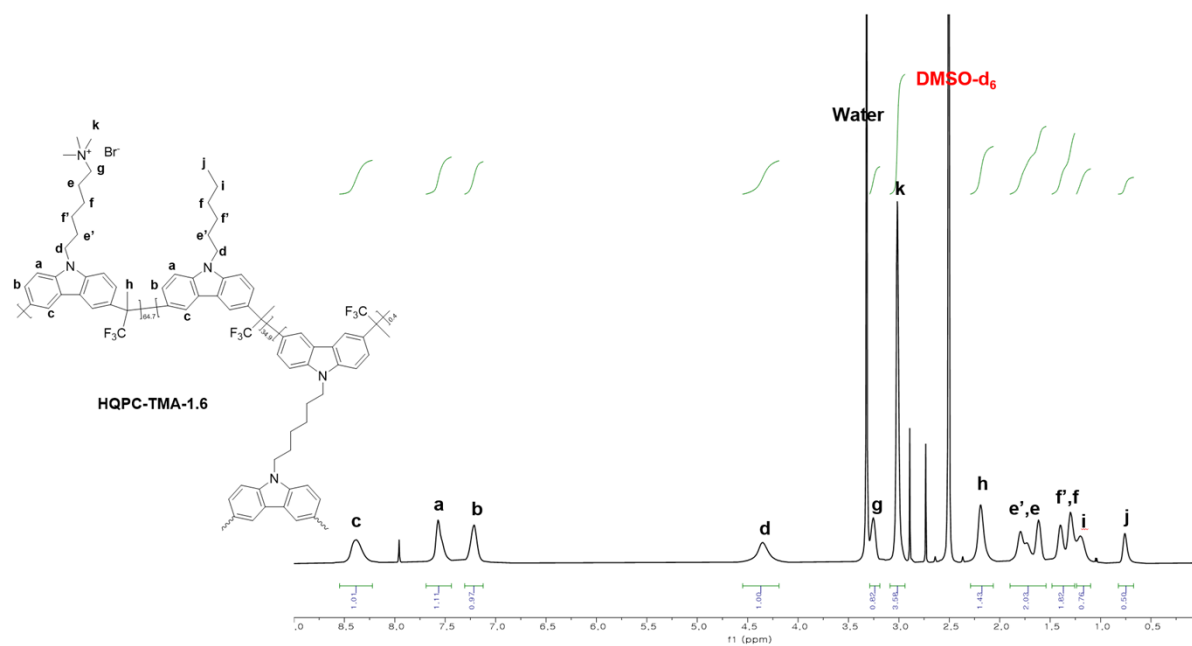
Fig. S9 ^{1}H NMR spectrum of HQPC-TMA-1.6

14
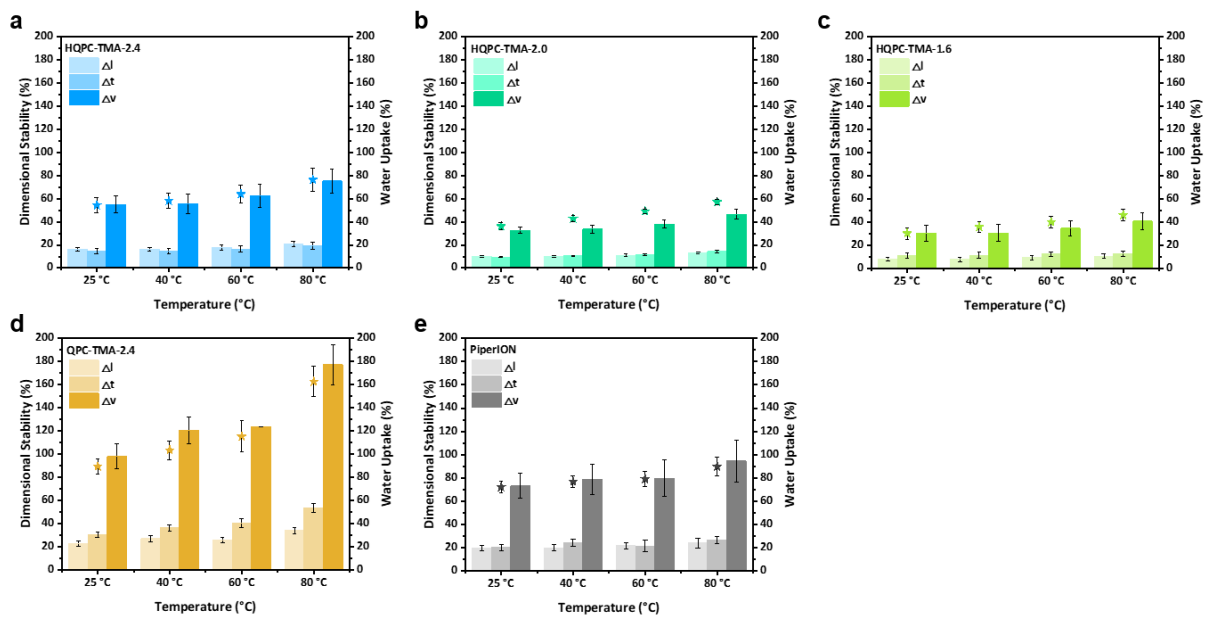
Fig. S10 Dimensional change and water uptake of tested AEMs with different temperatures. (a) HQPC-TMA-2.4 (b) HQPC-TMA-2.0 (c) HQPC-TMA-1.6 (d) QPC-TMA-2.4 (e) PiperION
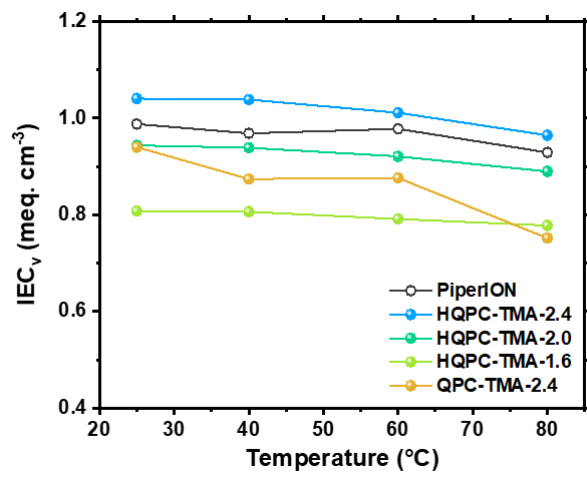
Fig. S11 The value of IECv of AEMs used in this work
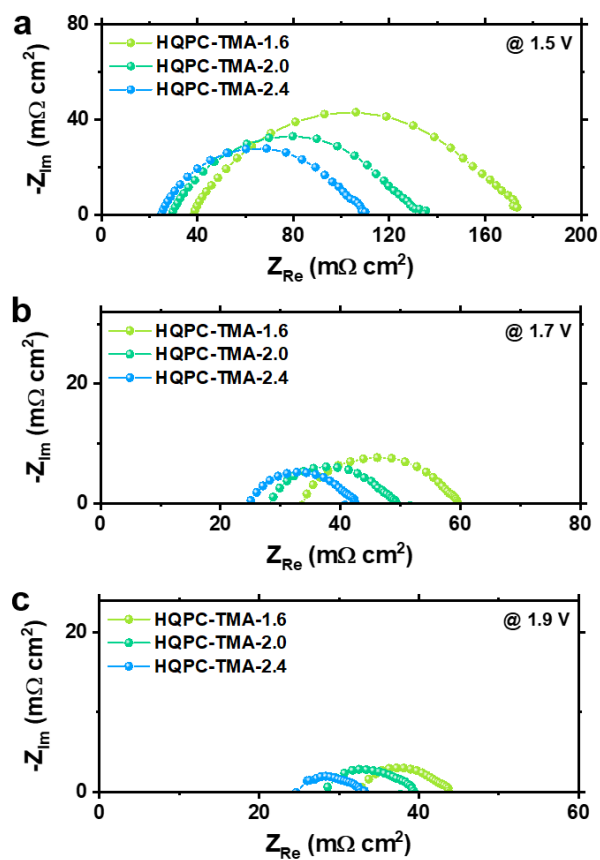
Fig. S12 EIS spectra measured at (a) 1.5 V, (b) 1.7 V, and (c) 1.9 V of the 1.0 M KOH-fed AEMWEs (80 ℃) with different HQPC-TMA-x AEMs. The detailed conditions of each cell are summarised in **Table S2**.
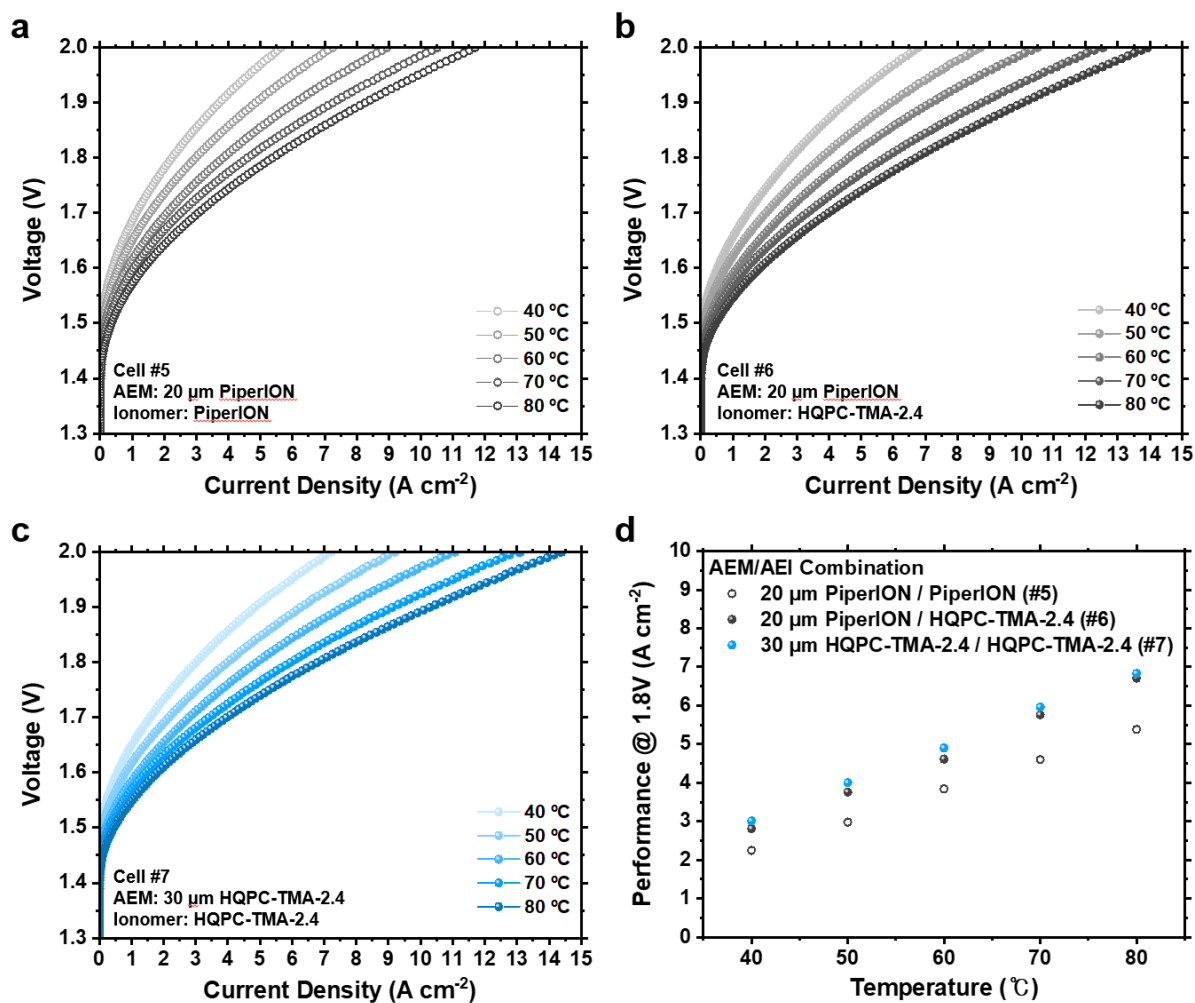
Fig. S13 (a-c) The I-V polarization of 1.0 M KOH-fed AEMWEs with different AEM/AEI combination at various operating temperatures. (d) Comparison of current densities at 1.8 V of tested 1.0 M KOH-fed AEMWEs at various operating temperatures. The detailed conditions of each single cell are summarised in **Table S3**.
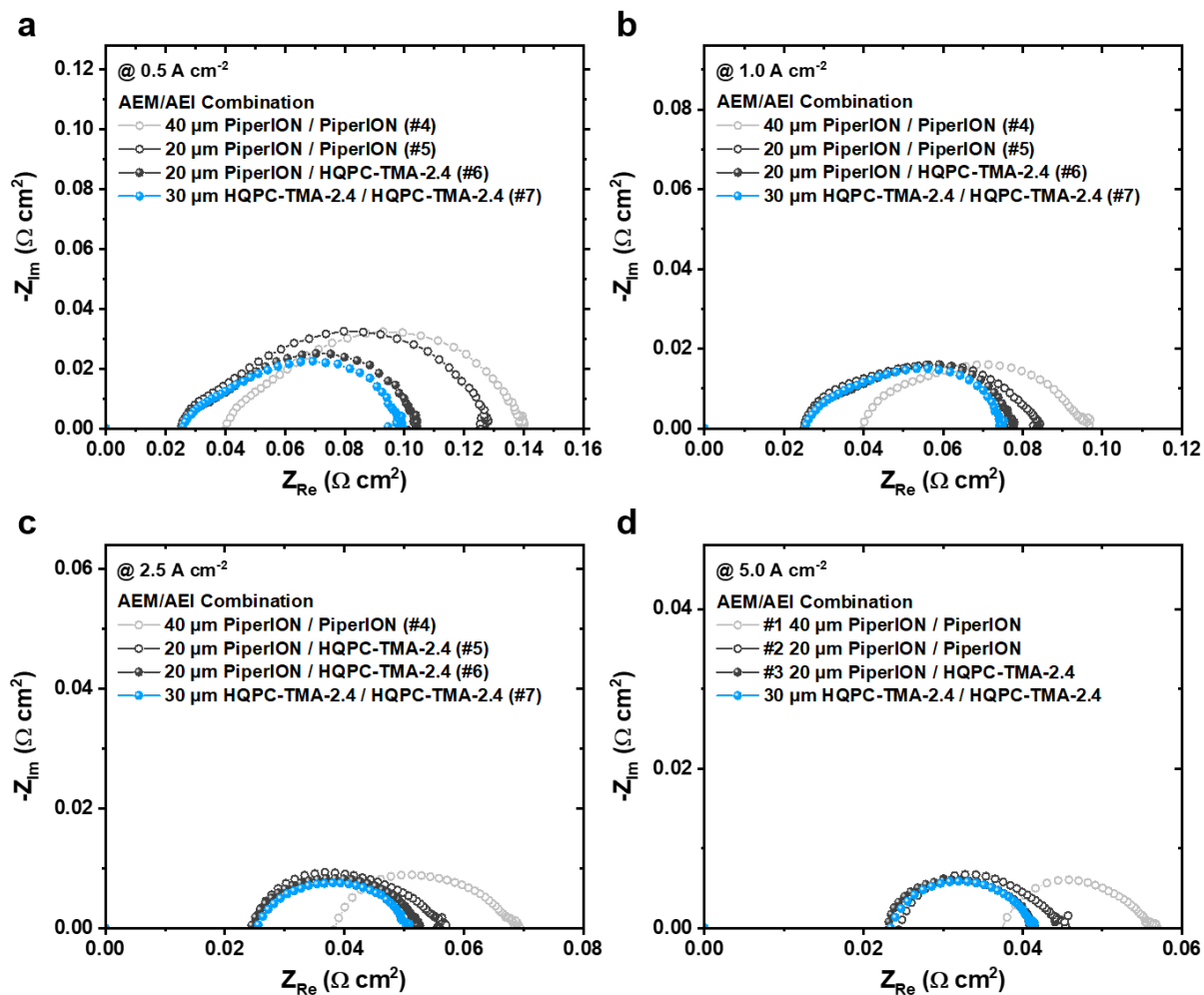
Fig. S14 EIS spectra measured at (a) 0.5 A cm⁻², (b) 1.0 A cm⁻², (c) 2.5 A cm⁻², and (d) 5.0 A cm⁻² of the 1.0 M KOH-fed AEMWEs (80 °C) with different HQPC-TMA-x AEMs. The detailed conditions of each single cell are summarised in **Table S3**.
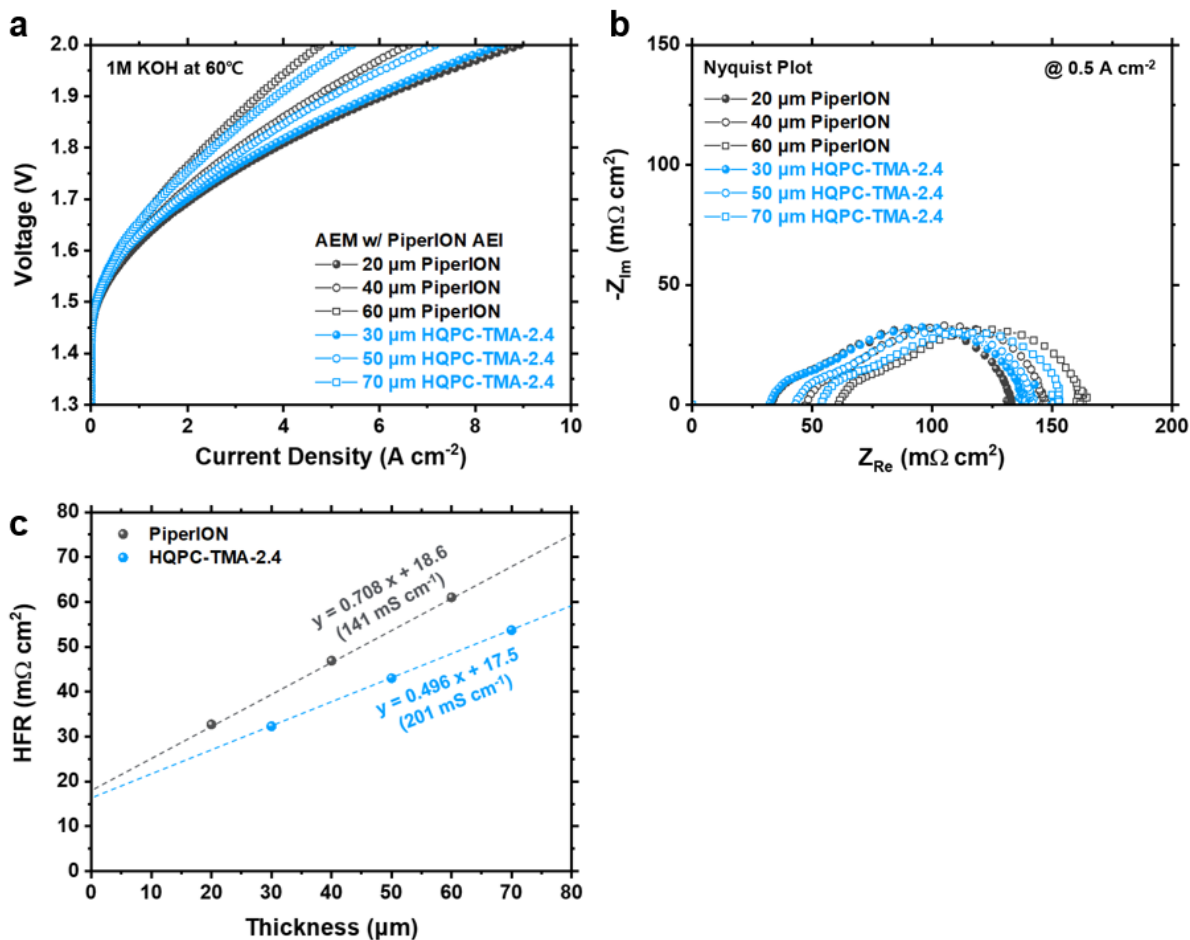
Fig. S15 (a) I–V polarisation curves and (b) electrochemical impedance spectra of 1.0 M KOH-fed electrolysers based on PiperION or HQPC-TMA AEMs with different thickness. (c) Measured HFR against the membrane thickness. The detailed conditions of each single cell are summarised in **Table S6**.

This experiment demonstrated a linear relationship between membrane thickness and HFR, allowing us to calculate through-plane conductivity accurately. As a result, HQPC-TMA-2.4 exhibited superior through-plane conductivity (201 mS cm^{-1} compared to PiperION's 141 mS cm^{-1}) at 60 ℃ in 1.0 M KOH feed condition, clarifying the similar R_{ohm} values observed in operational settings. The y-intercepts (~ 18 mΩ cm^2) in **Fig. S15c** represents the remaining resistive elements excluding the ion transport resistance through the AEM. (electrical resistances of other cell components and contact resistances between cell components)
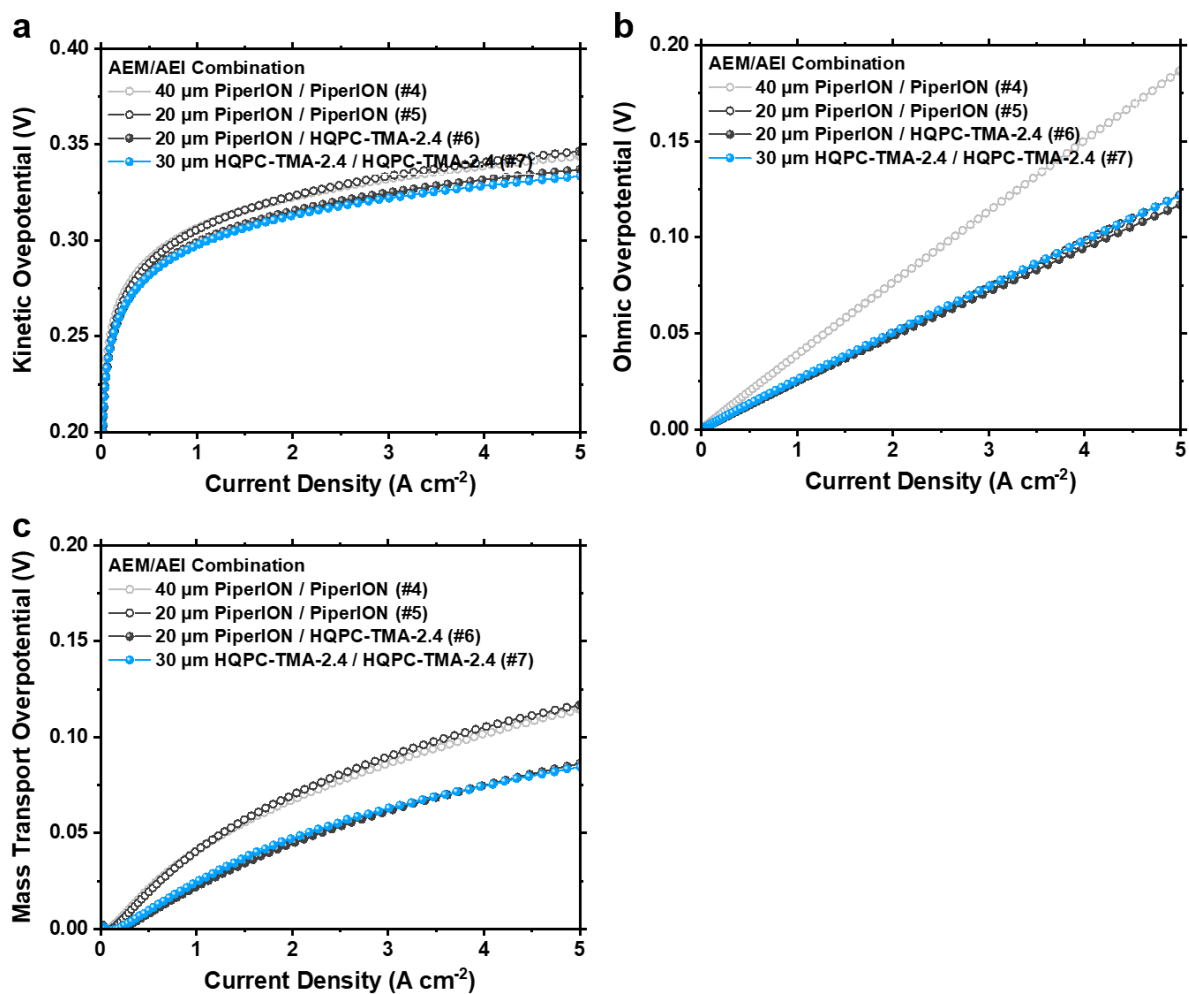
Fig. S16 Calculated overpotentials of the 1.0 M KOH-fed AEMWEs (80 °C) with different AEM/AEI combinations. (a) Kinetic overpotential, (b) ohmic overpotential, and (c) mass-transport overpotential. The detailed conditions of each cell are summarised in **Table S3**.
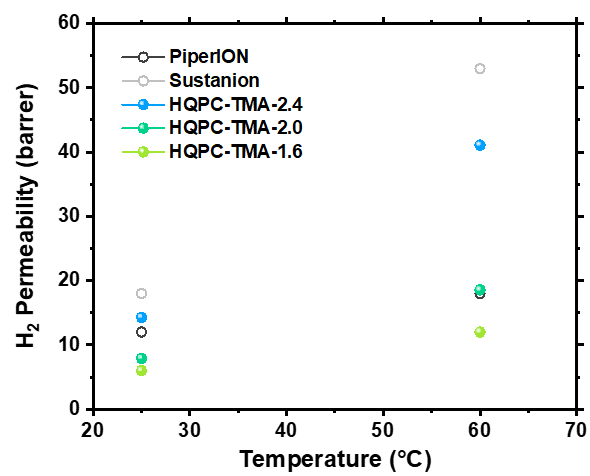
Fig. S17 Gas permeability of AEMs used in this work
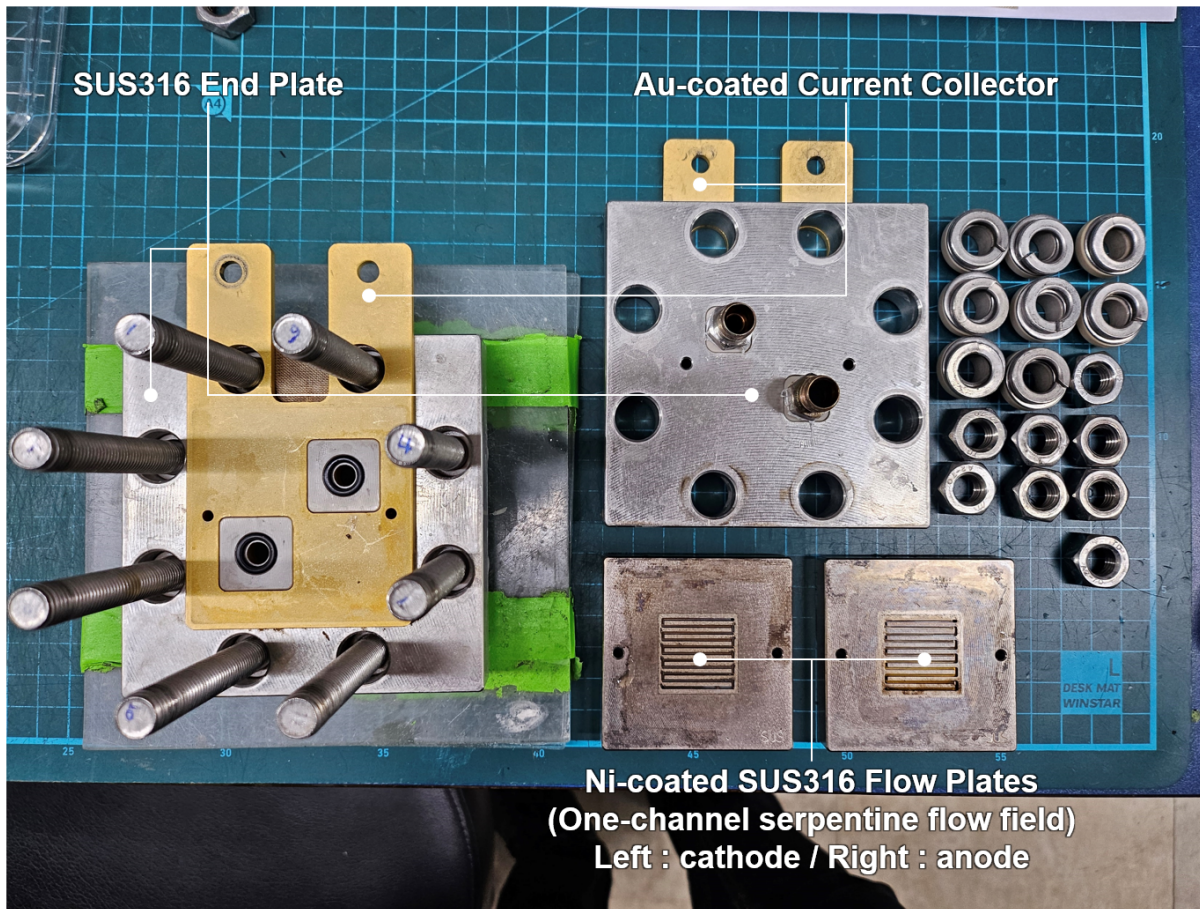
Fig. S18 Photo of the single-cell hardware used for AEMWE performance and durability evaluation, which taken after durability test.
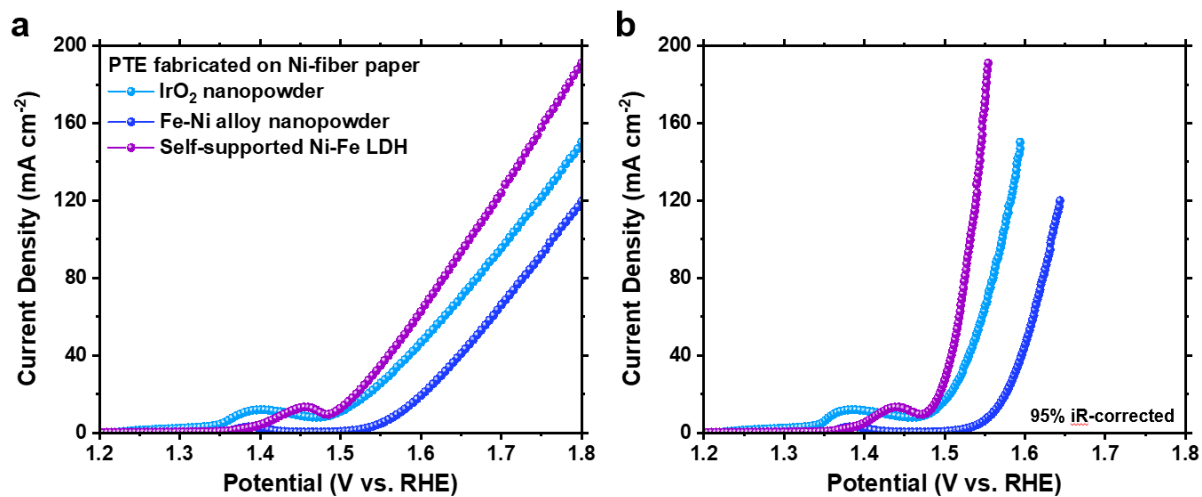
Fig. S19 Oxygen evolution reaction (OER) activities of porous transport electrodes (PTEs) fabricated on Ni-fiber paper (Dioxide Materials, USA) with different catalysts in 1.0 M KOH at room temperature. (a) No iR-correction (b) 95% iR-correction.
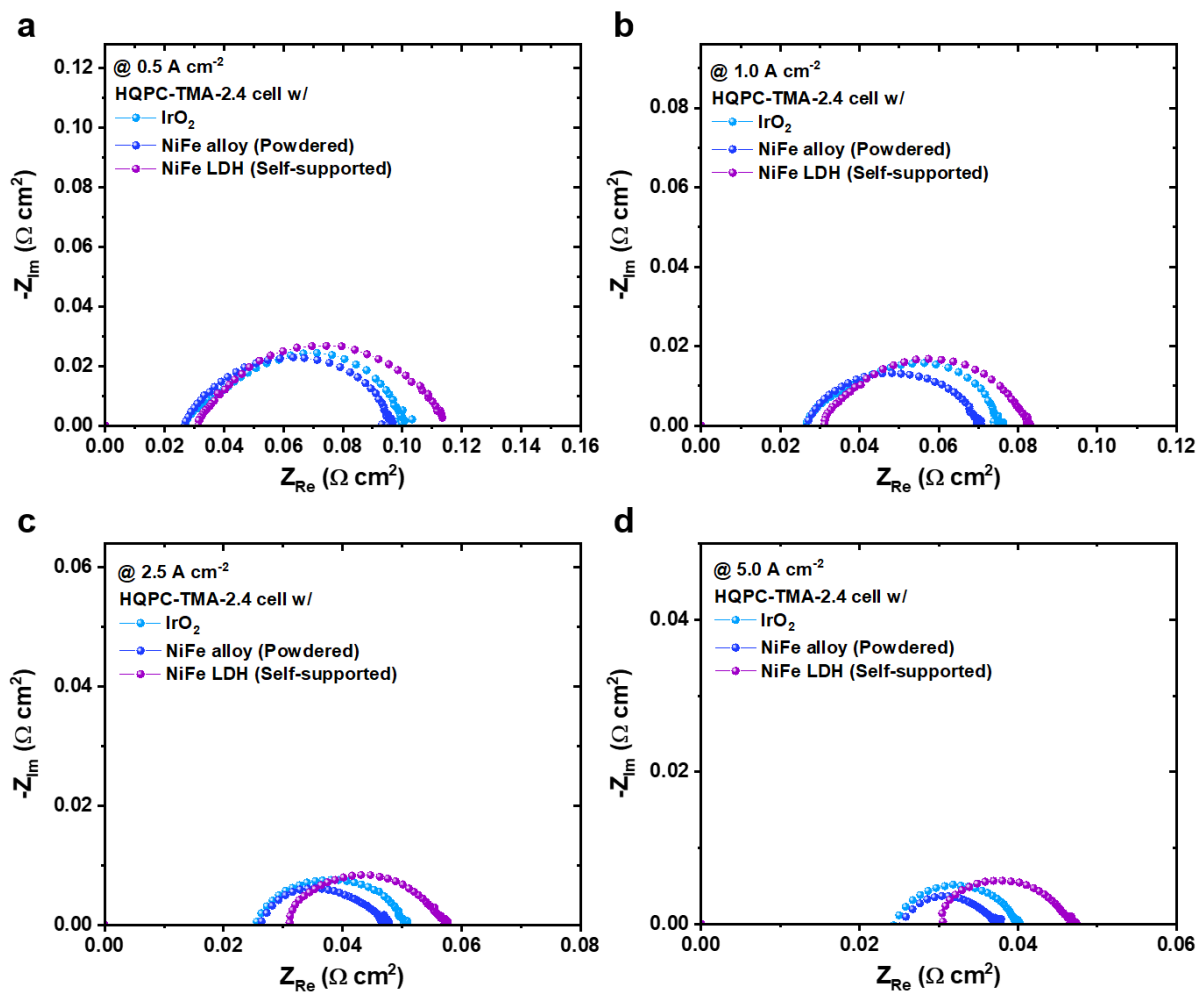
Fig. S20 EIS spectra measured at (a) 0.5 A cm^{-2}, (b) 1.0 A cm^{-2}, (c) 2.5 A cm^{-2}, and (d) 5.0 A cm^{-2} of the 1.0 M KOH-fed AEMWEs (80 °C) with HQPC-TMA-2.4-based electrolysers with different anodes. The detailed conditions of each cell summarised in **Table S4**.
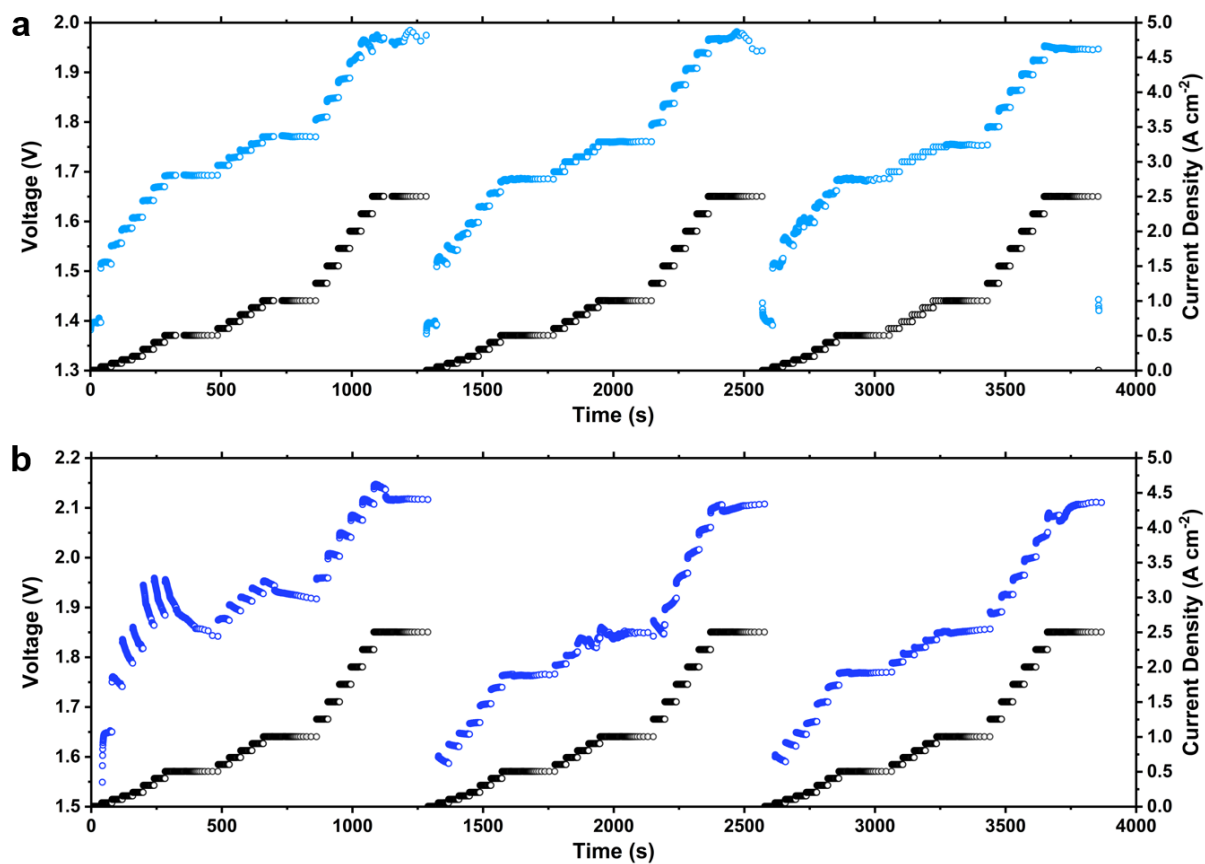
Fig. S21 Voltage and current density changes over time of pure-water-fed HQPC-TMA-2.4 cells with (a) PGM anode and (b) non-PGM anode during current-step process.
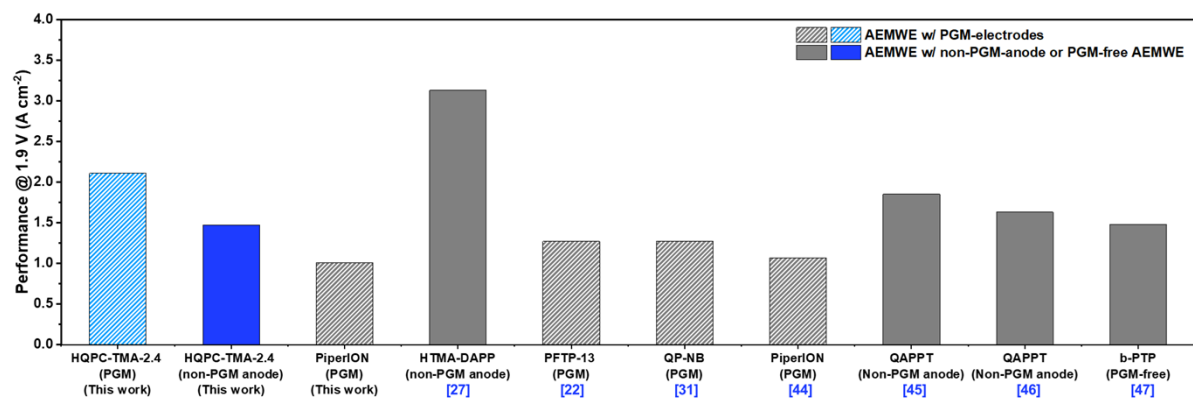
Fig. S22 Comparison of the cell performance of pure-water-fed AEMWE at 1.9 V reported in the literature[6-12].
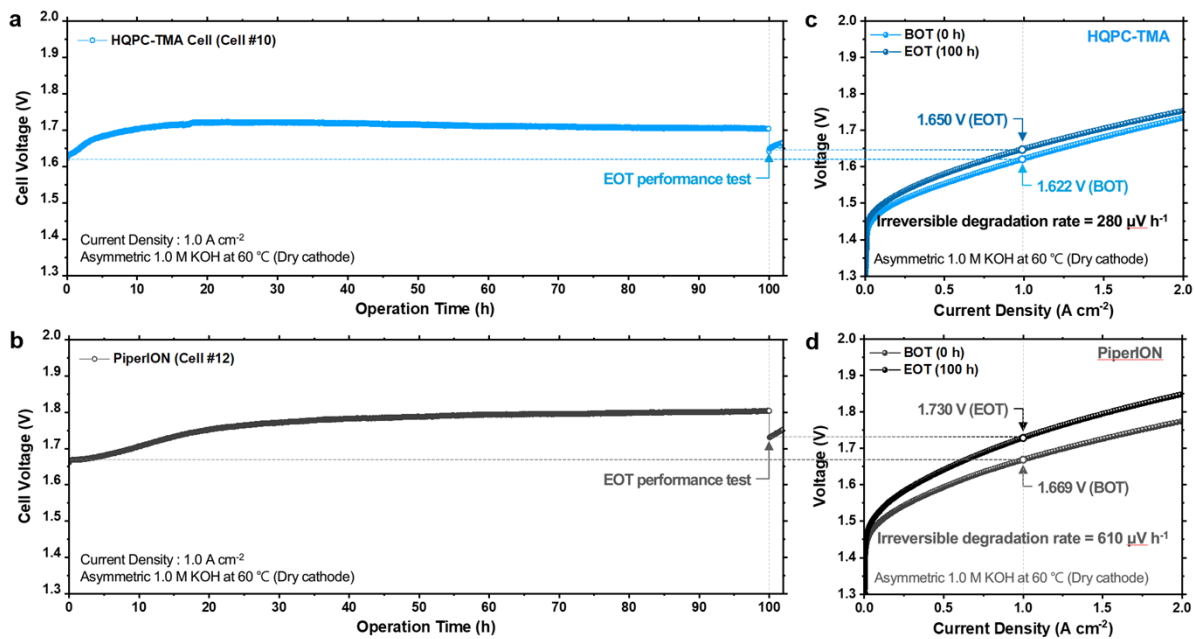
Fig. S23 Short-term durability of asymmetric 1.0 M KOH-fed AEMWE (dry-cathode) under 1.0 A cm^{-2} at 60 ℃ for 100 h. (a-b) Cell voltage changes during durability test and (c-d) I-V polarization of the asymmetric 1.0 M KOH-fed AEMWEs (dry-cathode) at 60 ℃ before and after durability test. The detailed conditions of each cell summarised in **Table S5**.
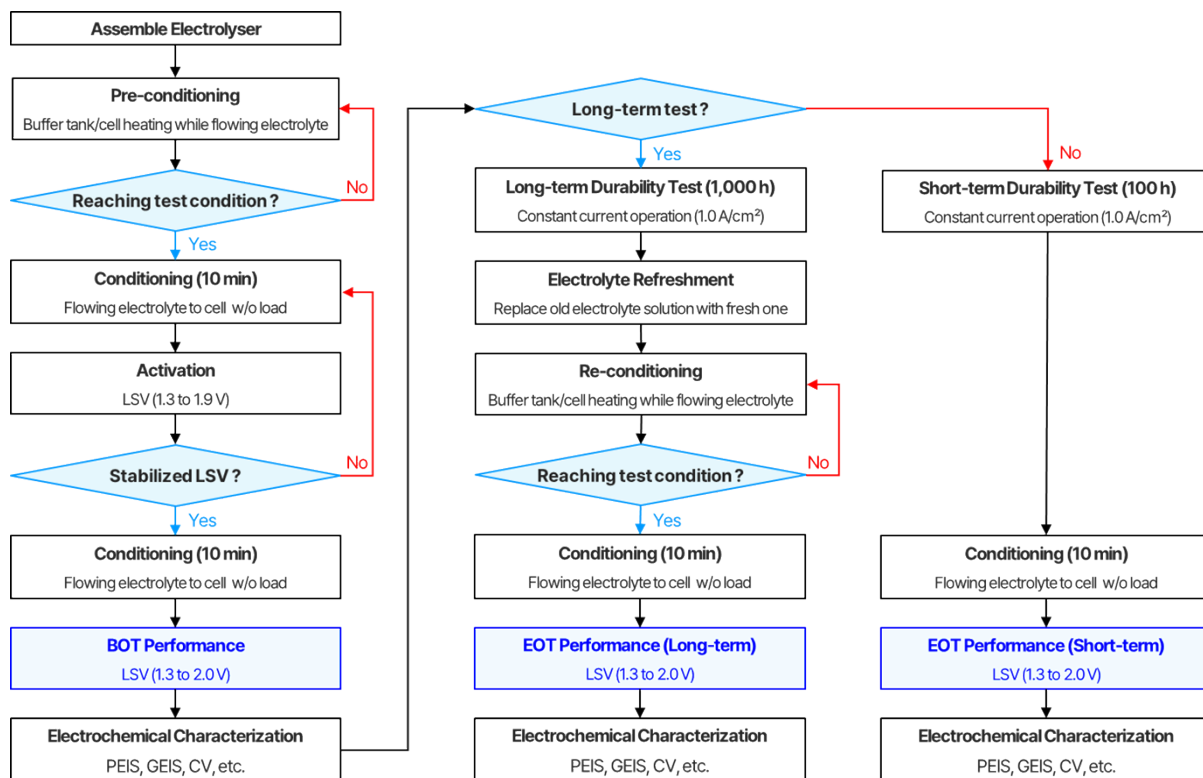
Fig. S24 Flowchart for AEMWE performance and *in situ* durability testing
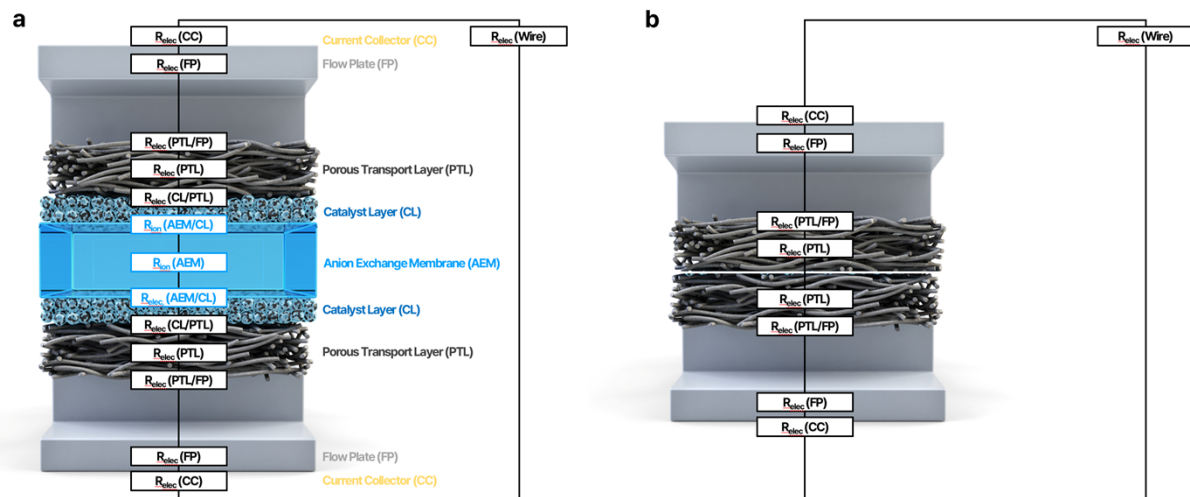
Fig. S25. Resistive components contributing to high-frequency resistance (HFR) in (a) a water electrolysis cell test setup and (b) a R_{others} measurement cell setup.

Supplementary Tables

Table S1. GPC data of PC-br-2.4 and HPC-br-x's

Polymer	M_n (kDa)	M_w (kDa)	PDI
HPC-br-2.4	65	307	4.7
HPC-br-2.0	89	343	3.9
HPC-br-1.6	78	312	4
PC-br-2.4	23	87	3.8

GPC measured at 40 °C in THF as eluent. (0.7 mg mL^{-1})

Table S2. Detailed condition of AEMWE single-cells with different HQPC-TMA-x AEMs.

Cell Component	Cell #1	Cell #2	Cell #3
Anode Gasket	PTFE Film Gasket (270 um)		
Anode PTL	Dioxide Ni Fiber Paper		
Anode Catalyst	IrO$_2$ (Active material loading of 2.0 mg$_{IrO2}$ cm^{-2})		
Anode Ionomer	HQPC-TMA-2.4 (Weight ratio of ionomer to catalyst = 20 wt.%)		
Membrane	HQPC-TMA-1.6 (30 μm)	HQPC-TMA-2.0 (30 μm)	HQPC-TMA-2.4 (30 μm)
Cathode CL	60 wt.% PtRu/C (Active material loading of 0.5 mg$_{PuRu}$ cm^{-2})		
Cathode Ionomer	HQPC-TMA-2.4 (Weight ratio of ionomer to catalyst = 20 wt.%)		
Cathode PTL	Carbon Paper w/ MPL (JNT30-A3)		
Cathode Gasket	PTFE Film Gasket (220 um)		

Table S3. Detailed condition of AEMWE single-cells with different AEM/AEI combination.

Cell Component	Cell #4	Cell #5	Cell #6	Cell #7
Anode Gasket	PTFE Film Gasket (270 um)			
Anode PTL	Bekaert stainless-steel 316 (SUS316) fiber paper (10AL3)			
Anode Catalyst	IrO_2 (Active material loading of 2.0 mg_{IrO2} cm^{-2})			
Anode Ionomer	PiperION (Weight ratio of ionomer to catalyst = 7.5 wt.%)		HQPC-TMA-2.4 (Weight ratio of ionomer to catalyst = 10 wt.%)	
Membrane	PiperION (40 μm)	PiperION (20 μm)	PiperION (20 μm)	HQPC-TMA-2.4 (30 μm)
Cathode CL	60 wt.% PtRu/C (Active material loading of 0.5 mg_{PuRu} cm^{-2})			
Cathode Ionomer	PiperION (Weight ratio of ionomer to catalyst = 20 wt.%)		HQPC-TMA-2.4 (Weight ratio of ionomer to catalyst = 20 wt.%)	
Cathode PTL	Carbon Paper w/ MPL (JNT30-A3)			
Cathode Gasket	PTFE Film Gasket (220 um)			

Table S4. Detailed condition of AEMWE single-cells with different anodes.

Cell Component	Cell #3	Cell #8	Cell #9
Anode Gasket	PTFE Film Gasket (270 um)		
Anode PTL	Dioxide Ni Fiber Paper		
Anode Catalyst	IrO_2 (Active material loading of 2.0 mg_{IrO2} cm^{-2})	Fi-Ni alloy (Active material loading of 1.0 mg_{IrO2} cm^{-2})	Self-supported-type Ni-Fe LDH
Anode Ionomer	HQPC-TMA-2.4 (Weight ratio of ionomer to catalyst = 10 wt.%)		-
Membrane	HQPC-TMA-2.4 (30 μm)		
Cathode CL	60 wt.% PtRu/C (Active material loading of 0.5 mg_{PuRu} cm^{-2})		
Cathode Ionomer	HQPC-TMA-2.4 (Weight ratio of ionomer to catalyst = 20 wt.%)		
Cathode PTL	Carbon Paper w/ MPL (JNT30-A3)		
Cathode Gasket	PTFE Film Gasket (220 um)		

Table S5. Detailed condition of AEMWE single-cells with PGM or PGM-free electrodes for in-situ durability test.

Cell Component	Cell #10	Cell #11	Cell #12
Anode Gasket	PTFE Film Gasket (270 um)	PTFE Film Gasket (520 um)	PTFE Film Gasket (270 um)
Anode PTL	Dioxide Ni Fiber Paper	Dioxide SUS316 Fiber Paper	Dioxide Ni Fiber Paper
Anode Catalyst	IrO_2 (Active material loading of 2.0 mg_{IrO2} cm^{-2})	NiFeCo (Active material loading of 2.0 mg_{NiFeCo} cm^{-2})	IrO_2 (Active material loading of 2.0 mg_{IrO2} cm^{-2})
Anode Ionomer	HQPC-TMA-1.6 (Weight ratio of ionomer to catalyst = 10 wt.%)	Nafion (Weight ratio of ionomer to catalyst = 9.3 wt.%)	PiperION (Weight ratio of ionomer to catalyst = 7.5 wt.%)
Membrane	HQPC-TMA-2.4 (50 μm)		PiperION (40 μm)
Cathode CL	60 wt.% PtRu/C (Active material loading of 0.5 mg_{PuRu} cm^{-2})	$NiFe_2O_4$ (Active material loading of 2.0 $mg_{NiFe2O4}$ cm^{-2})	60 wt.% PtRu/C (Active material loading of 0.5 mg_{PuRu} cm^{-2})
Cathode Ionomer	HQPC-TMA-1.6 (Weight ratio of ionomer to catalyst = 20 wt.%)	Nafion (Weight ratio of ionomer to catalyst = 9.3 wt.%)	PiperION (Weight ratio of ionomer to catalyst = 20 wt.%)
Cathode PTL	Carbon Paper w/ MPL (JNT30-A3)	Dioxide Ni Fiber Paper	Carbon Paper w/ MPL (JNT30-A3)
Cathode Gasket	PTFE Film Gasket (220 um)	PTFE Film Gasket (270 um)	PTFE Film Gasket (220 um)

Table S6. Detailed condition of AEMWE single-cells with different AEM thickness.

Cell Component	Cell #4	Cell #5	Cell #13	Cell #14	Cell #15	Cell #16
Anode Gasket	PTFE Film Gasket (270 um)					
Anode PTL	Bekaert stainless-steel 316 (SUS316) fiber paper (10AL3)					
Anode Catalyst	IrO$_2$ (Active material loading of 2.0 mg$_{IrO2}$ cm^{-2})					
Anode Ionomer	PiperION (Weight ratio of ionomer to catalyst = 7.5 wt.%)					
Membrane	PiperION (40 μm)	PiperION (20 μm)	PiperION (60 μm)	HQPC-TMA-2.4 (30 μm)	HQPC-TMA-2.4 (50 μm)	HQPC-TMA-2.4 (70 μm)
Cathode CL	60 wt.% PtRu/C (Active material loading of 0.5 mg$_{PuRu}$ cm^{-2})					
Cathode Ionomer	PiperION (Weight ratio of ionomer to catalyst = 20 wt.%)					
Cathode PTL	Carbon Paper w/ MPL (JNT30-A3)					
Cathode Gasket	PTFE Film Gasket (220 um)					

References

1   M. S. Cha, J. E. Park, S. Kim, S.-H. Han, S.-H. Shin, S. H. Yang, T.-H. Kim, D. M. Yu, S. So, Y. T. Hong, S. J. Yoon, S.-G. Oh, S. Y. Kang, O.-H. Kim, H. S. Park, B. Bae, Y.-E. Sung, Y.-H. Cho and J. Y. Lee, *Energy Environ. Sci.*, 2020, **13**, 3633-3645.

2   S. H. Yang, W. Jung, H. Lee, S.-H. Shin, S. J. Lee, M. S. Cha, W. Choi, S.-G. Oh, K. B. Lee, U. Lee, D. H. Won, and J. Y. Lee, *ACS Energy Lett.*, 2023, **8**, 1976-1984.

3   J. Y. Lee, D. M. Yu, T.-H. Kim, S. J. Yoon, and Y. T. Hong, *J. Membr. Sci.*, 2015, **492**, 209-219.

4   M. S. Cha, J. E. Park, S. Kim, S.-H. Shin, S. H. Yang, S. J. Lee, T.-H. Kim, D. M. Yu, S. So, K. M. Oh, Y.-E. Sung, Y.-H. Cho and J. Y. Lee, *J. Mater. Chem. A*, 2022, **10**, 9693-9706.

5   M. Mandal, G. Huang, and P. A. Kohl, *J. Memb. Sci.*, 2019, **570-571**, 394-402.

6   G. A. Lindquist, S. Z. Oener, R. Krivina, A. R. Motz, A. Keane, C. Capuano, K. E. Ayers, and S. W. Boettcher, *ACS Appl. Mater Interfaces*, 2021, **13**, 51917-51924.

7   N. Chen, S. Y. Paek, J. Y. Lee, J. H. Park, S. Y. Lee, and Y. M. Lee, *Energy Environ. Sci.*, 2021, **14**, 6338-6348.

8   D. P. Leonard, M. Lehmann, J. M. Klein, I. Matanovic, C. Fujimoto, T. Saito, and Y. S. Kim, *Adv. Energy Mater.*, 2023, **13**, 2203488.

9   L. Wan, J. Liu, Z. Xu, Q. Xu, M. Pang, P. Wang, and B. Wang, *Small*, 2022, **18**, 2200380.

10 B. Huang, X. Wang, W. Li, W. Tian, L. Luo, X. Sun, G. Wang, L. Zhuang, and L. Xiao, *Angew. Chem. Int. Ed.*, 2023, **62**, e202304230.

11 Y. Zheng, A. Serban, H. Zhang, N. Chen, F. Song, and X. Hu, *ACS Energy Lett.*, 2023, **8**, 5018-5024.

12 D. Li, E. J. Park, W. Zhu, Q. Shi, Y. Zhou, H. Tian, Y. Lin, A. Serov, B. Zulevi, E. D. Baca, C. Fujimoto, H. T. Chung, and Y. S. Kim, *Nat. Energy*, 2020, **5**, 378-385.